Energy dependence of the optical potential for the $^{16}O+^{144}Sm$ system near the Coulomb barrier

D. Abriola, D. DiGregorio, J. E. Testoni, A. Etchegoyen, M. C. Etchegoyen, J. O. Fernández Niello, A. M. J. Ferrero, S. Gil, A. O. Macchiavelli, A. J. Pacheco, and J. Kittl

TANDAR, Departamento de Física, Comisión Nacional de Energía Atómica, Buenos Aires, Argentina

(Received 11 May 1988)

Angular distributions for elastic and inelastic scattering of $^{16}O+^{144}Sm$ have been measured at bombarding energies $E=69.2$ and 72.3 MeV. Excitation functions were measured between $E=61$ and 76.3 MeV at backward angles. The present elastic scattering data plus existing fusion data were adjusted with both energy-independent and energy-dependent optical-model potentials. The energy dependence appears to be consistent with the dispersion relations which correlate the real and imaginary components of the potentials. The potentials behave similarly when coupling to inelastic channels is considered.

I. INTRODUCTION

The enhancement of the fusion cross section below the Coulomb barrier has been the subject of great theoretical and experimental interest.[1,2] It has been attributed to a lowering of the barrier due to the coupling to inelastic and transfer degrees of freedom[3–5] or to static deformation of the nuclei.[6,7]

The first step of such descriptions is the calculation of the fusion cross sections with a "bare" potential usually taken from systematic studies of elastic scattering data at energies well above the barrier. The result is a fusion cross section that is in agreement with data above the barrier while it underpredicts the data below the barrier. Their second step is the consideration of static deformation and surface excitations which are taken into account either schematically[4,8] or with a full quantum-mechanical calculation.[3,5] When this is performed a good agreement with the fusion data is obtained.

In spite of the success of those models in accounting for the subbarrier enhancement of the fusion cross sections, recent studies of direct reaction cross sections and fusion cross sections have shown that (a) the potentials from systematics do not adjust the elastic scattering data at energies near the Coulomb barrier,[9,10] and (b) the potentials have to be energy dependent in the vicinity of the Coulomb barrier.[11,12]

The $^{16}O+^{144}Sm$ system has been selected since it minimizes the influence of static and dynamic deformations and allows a simple evaluation of the effect of the bare nuclear potential.

The elastic and inelastic scattering in the system $^{16}O+^{144}Sm$ has been measured as a part of a study on fusion and quasielastic reactions near the Coulomb barrier. For this system there are recent data on fusion excitation functions[7] and transfer angular distributions.[13] In this work a simultaneous description of the elastic scattering data and the fusion data is presented. The importance of using energy-dependent optical-model potentials, whose real and imaginary parts are linked through the dispersion relations, is stressed by comparison with calculations performed with energy-independent potentials.

II. EXPERIMENTAL METHOD

Beams of ^{16}O with energies ranging from 61 to 76.3 MeV provided by the 20 UD tandem accelerator at the TANDAR laboratory in Buenos Aires were used to bombard a 94 $\mu g/cm^2$ ^{144}Sm target, enriched to 88.6% and supported on a 30 $\mu g/cm^2$ carbon backing.

The reaction products were detected using five 150 μm surface barrier Si counters. Their energy resolution was $\Delta E \simeq 700-800$ keV. The angular uncertainty was estimated to be $\Delta\theta_{lab} \simeq \pm 0.3°$, and the angular acceptance varied from $\pm 0.3°$ to $\pm 0.8°$. A monitor detector was placed at 20° for normalization.

A typical energy spectrum at $E=69.2$ MeV and $\theta_{c.m.}=150°$ is shown in Fig. 1; the elastic peak is well separated from the inelastic, which is the sum of the unresolved 2^+ (1.66 MeV) and 3^- (1.81 MeV) states of ^{144}Sm. Although no direct charge identification was performed in this experiment, transfer reactions can be easily separated from elastic and inelastic scattering because they contribute to different regions of the energy spectra. Figure 1 shows the position of the peaks corresponding to the transfer channels $^{144}Sm(^{16}O,^{17}O)$ and $^{144}Sm(^{16}O,^{12}C)$, which lie about 6.4 MeV below the elastic peak, together with that corresponding to the inelastic scattering $^{144}Sm(^{16}O,^{16}O^*(3^-, 6.13\ MeV))$.

Angular distributions were taken at $E=69.2$ and 72.3 MeV for center-of-mass angles between $\theta_{c.m.}=40°$ and 170°. The excitation functions at two fixed angles, $\theta_{c.m.}=137.1°$ and 154.3°, were measured in the energy range $E=61-76.3$ MeV (the Coulomb barrier, in the laboratory frame, is $V_c \cong 66.7$ MeV).

The measured angular distributions for elastic scattering at $E=72.3$ and 69.2 MeV together with existing data

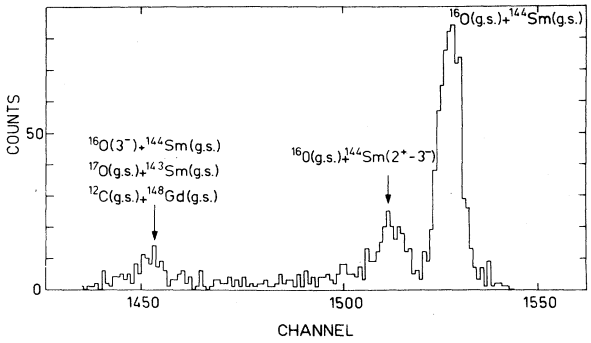

FIG. 1. Energy spectrum of the reaction products for $^{16}O+^{144}Sm$, measured at $E=69.2$ MeV and $\theta_{c.m.}=150°$. Exit channels are indicated.

taken at $E=66$ MeV (Ref. 14) are shown in Fig. 2. For angles smaller than $\theta_{c.m.}=110°$ the elastic and inelastic peaks were not resolved. Therefore, in this angular range the differential cross sections for the elastic scattering include a small contribution ($<5\%$) due to the inelastic channel.

The main contributions to uncertainties in the evaluation of cross sections arise from (a) the unfolding procedure of the elastic and inelastic peaks, background substraction, and statistical errors (the error bars of the figures take into account all these factors); and (b) systematic errors arising from uncertainties in the position of the monitor, in the evaluation of solid angles, and in the contribution of target contaminants to the peaks of interest. These systematic errors are estimated to be around 12% for the elastic and 20% for the inelastic scattering data. The presence of target contaminants is not an important source of error. This error was estimated to be about 2% from the known abundance of those contaminants and the measured elastic angular distributions for ^{148,152}Sm.[6]

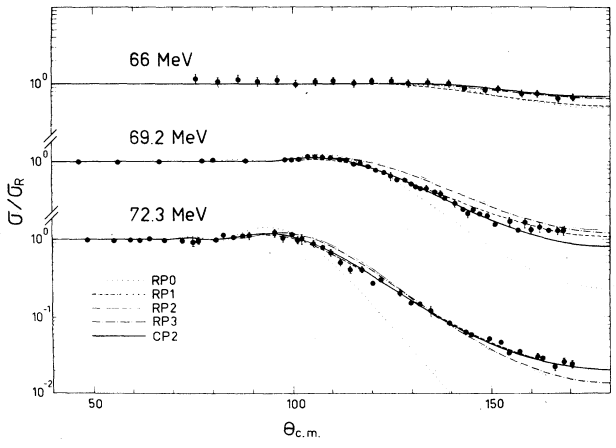

FIG. 2. Elastic scattering angular distributions for $^{16}O+^{144}Sm$. The lines are optical-model fits with different potentials as explained in the text. The angular distribution at $E=66$ MeV is taken from Ref. 14.

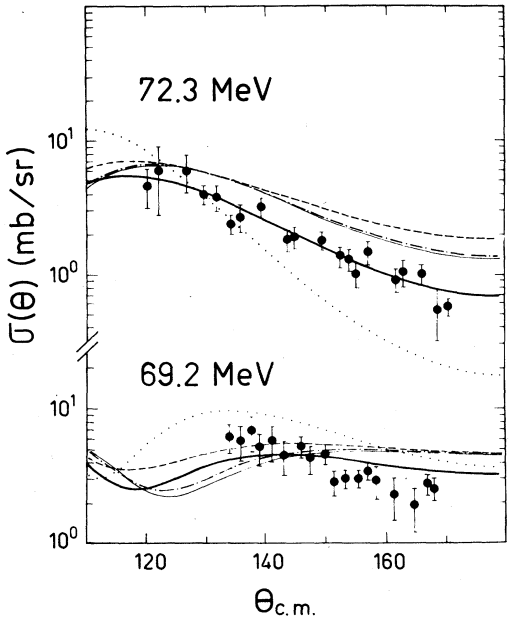

FIG. 3. Inelastic-scattering angular distributions for $^{16}O+^{144}Sm$. The lines are DWBA calculations with different potentials (see Fig. 2 for notation).

The measured angular distributions for the inelastic scattering at $E=69.2$ and 72.3 MeV are shown in Fig. 3. The tails of the elastic peaks, for angles $110°<\theta_{c.m.}<133°$ in the first case and $110°<\theta_{c.m.}<120°$ in the second case, give errors greater or equal to the magnitude of the cross sections. Therefore these angular ranges are omitted from Fig. 3.

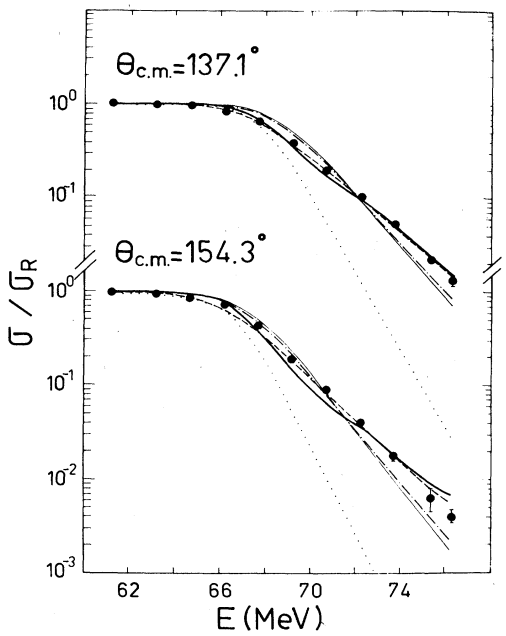

FIG. 4. Elastic-scattering excitation functions for $^{16}O+^{144}Sm$. The lines are optical-model fits (see Fig. 2 for notation).

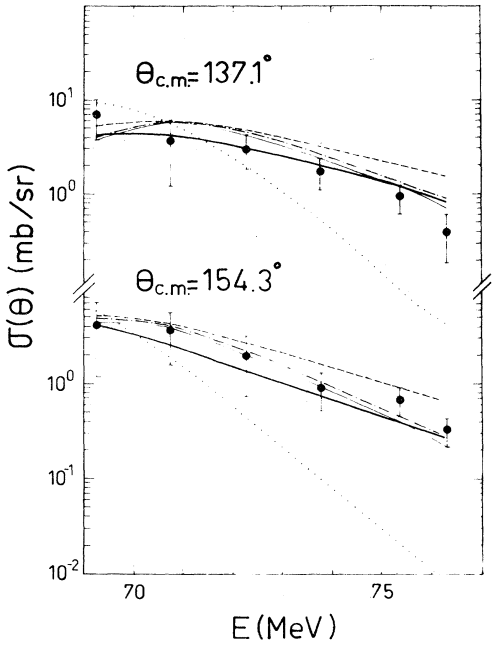

FIG. 5. Inelastic-scattering excitation functions for $^{16}O+^{144}Sm$. The lines are DWBA calculations (see Fig. 2 for notation).

The elastic scattering excitation functions measured at $\theta_{c.m.}=137.1°$ and 154.3° are presented in Fig. 4. The inelastic scattering excitation functions at the same angles are displayed in Fig. 5; in this case the points in the range $61<E<69.3$ MeV were eliminated due to the errors caused by the tail of the elastic peak.

III. OPTICAL-MODEL ANALYSIS

A. Energy-independent potentials

In an attempt to simultaneously describe the elastic scattering and the fusion data[7] energy-independent optical potentials, labeled RP0, RP1, RP2, and RP3 with a Woods-Saxon shape for the real part were tested. Their parameters are shown in Table I. The square of a Woods-Saxon potential for the imaginary part, taken from Ref. 3, simulates the incoming wave boundary condition and accounts for fusion. The fusion cross sections are evaluated as

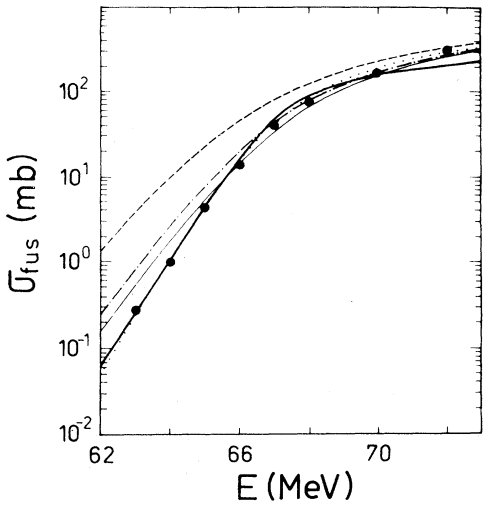

FIG. 6. Fusion excitation function for $^{16}O+^{144}Sm$ (taken from Ref. 7). The lines are explained in the text (see Fig. 2 for notation).

$$\sigma_{\text{fus}}=\pi\lambda^2\sum_l(2l+1)T_l^{\text{op}}\ ,$$

where T_l^{op} are the optical-model transmission coefficients. Elastic scattering calculations with the different potentials are displayed in Figs. 2 and 4, while the fusion cross sections calculated using those potentials are shown in Fig. 6.

The potentials RP0, RP1, RP2, and RP3 have no imaginary parts to simulate peripheral processes. Indeed the short-range imaginary potential used has no effect on the elastic cross sections besides accounting for an incoming wave condition (hence the notation: RP stands for real potential). Although this is a frequently adopted assumption to describe fusion,[3] it might not be adequate to describe elastic and inelastic scattering and it will be relaxed in Sec. III B.

The potential RP0 has a barrier described in the parabolic approximation by the parameters $r_B=1.42$ fm, $V_B=59.9$ MeV, and $\hbar\omega=4.01$ MeV, where r_B is the radius parameter, V_B the barrier height and $\hbar\omega$ the barrier width. This potential yields similar fusion cross sections to those calculated in Ref. 7 using a one-dimensional Wong's model[15] with barrier parameters $r_B=1.32$ fm,

TABLE I. Quality of the fits (χ^2/point) to elastic scattering and fusion data from different potentials.

	Potential[a]			χ^2/point					
				Angular distributions			Excitation functions		
	V (MeV)	r_0 (fm)	a (fm)	66 MeV	69.2 MeV	72.3 MeV	137.1°	154.3°	Fusion
RP0	64	1.18	0.75	1.3	19.8	37.0	36.7	39.9	3.0
RP1	202	1.32	0.30	1.3	1.6	0.7	0.3	1.1	2.8×10^4
RP2	289	1.18	0.46	0.4	19.1	5.9	6.7	5.3	8.6
RP3	102	1.27	0.41	0.3	12.3	4.4	4.4	3.6	7.4×10^2
CP2	b	1.18	0.46	0.3	1.0	0.8	1.0	4.5	4.4
CP3	b	1.27	0.41	0.4	1.7	0.9	2.3	3.6	14.3

[a]All potentials have a short-range volume imaginary component which is the square of a Woods-Saxon potential given by $W=10$ MeV, $ri_0=1$ fm, and $ai=0.4$ fm.

[b]The potentials CP2 and CP3 have energy-dependent V and WS. Their surface imaginary part has $rsi_0=1.48$ fm and $asi=0.131$ fm.

$V_B = 60$ MeV, and $\hbar\omega = 3.9$ MeV, in good agreement with fusion data. However, as is shown in Figs. 2 and 4, RP0 fails to reproduce the elastic scattering data.

The potential RP1 was obtained by fitting the elastic angular distribution at $E = 72.3$ MeV, searching in all the real-potential parameters. RP1 has a very small diffusivity ($a = 0.3$ fm) and a large radius parameter ($r_0 = 1.32$ fm) compared with standard parametrizations, such as the Akyuz-Winther potential[16] ($a = 0.656$ fm and $r_0 = 1.172$ fm). The barrier parameters for RP1 are $r_B = 1.51$ fm, $V_B = 59.48$ MeV, and $\hbar\omega = 6.85$ MeV. This potential gives reasonably good fits to the elastic angular distributions and excitation functions but fails to reproduce the fusion cross sections, which are grossly overestimated.

The potential RP2 was obtained by fitting the elastic angular distribution at $E = 72.3$ MeV varying V and a and keeping fixed the radius parameter, $r_0 = 1.18$ fm. The barrier parameters corresponding to RP2 are $r_B = 1.45$ fm, $V_B = 60.51$ MeV, and $\hbar\omega = 5.35$ MeV. This potential adjusts poorly the elastic data but gives a reasonable account of the fusion excitation function.

Finally RP3, a potential with radius and diffusivity parameters intermediate between RP1 and RP2 was obtained by fitting the elastic angular distribution at $E = 72.3$ MeV, adjusting only V. Its barrier parameters are $r_B = 1.47$ fm, $V_B = 60.30$ MeV, and $\hbar\omega = 5.81$ MeV. This potential, compared with RP1, produces a better adjustment of fusion and a worse adjustment of elastic scattering data. Conversely RP3, compared with RP2, gives a better account of elastic data and a worse account of fusion data.

B. Energy-dependent potentials

In this section two assumptions used up to now, namely, that the potentials are energy independent and that there is no surface imaginary potential to represent peripheral reactions (transfer and inelastic), are relaxed.

The importance of energy-dependent potentials near the Coulomb barrier for the description of both elastic and fusion data has been emphasized in connection with the dispersion relations in Ref. 12. This energy dependence arises from the fact that the imaginary potential which describes the inelastic and transfer channels should vanish below the Coulomb barrier, where these channels are essentially closed. The dispersion relations, which correlate the real and imaginary parts of the optical potential change, in turn, the real potential as a function of the energy.

This possibility was considered with a surface imaginary potential which takes into account the absorption due to peripheral processes, leaving the internal-volume imaginary potential to account for fusion. Its shape, as usual, is the derivative of a Woods-Saxon shape with depth, radius parameter, and diffusivity to be address as *WS*, rsi_0, and *asi*, respectively.

The adjustment was performed as follows.

(a) Starting with the energy-independent potential that gives the best overall results, RP3, a surface imaginary potential was added. The depth, radius parameter, and diffusivity of the surface imaginary potential were determined by adjusting the elastic angular distribution at $E = 72.3$ MeV.

(b) The values of rsi_0 and *asi* determined in (a) were fixed, whereas V and *WS* were adjusted at each energy.

(c) The real and imaginary parts of the potentials are evaluated at the strong absorption radius $R_s = 11.8$ fm.[17] The following schematic dependence of the surface imaginary potential at the strong absorption radius (WS_{R_s}) is used:

$$WS_{R_s}(E) = \begin{cases} 0 \text{ for } E < E_a \ , \\ W_0(E - E_a)/(E_b - E_a) \text{ for } E_a < E < E_b \ , \\ W_0 \text{ for } E > E_b \ , \end{cases}$$

where the parameters E_a, E_b, and W_0 are varied to adjust the real potential $V_{R_s}(E)$ using the dispersion relations given in Ref. 12:

$$V_{R_s}(E) = V_0 + \Delta V(E)$$

with

$$\Delta V(E) = \frac{W_0}{\pi}(\varepsilon_a \ln|\varepsilon_a| - \varepsilon_b \ln|\varepsilon_b|) \ ,$$

where

$$\varepsilon_i = (E - E_i)/(E_b - E_a) \ .$$

(d) The values of the energy-dependent potentials $V(E)$ and $WS(E)$ resulting from (c) are used to calculate the elastic scattering at the different energies and to evaluate the fusion cross sections. This is performed by using a model which calculates the fusion cross section using an incoming wave condition and the peripheral processes using the surface imaginary potential.[18] Figure 7 shows the

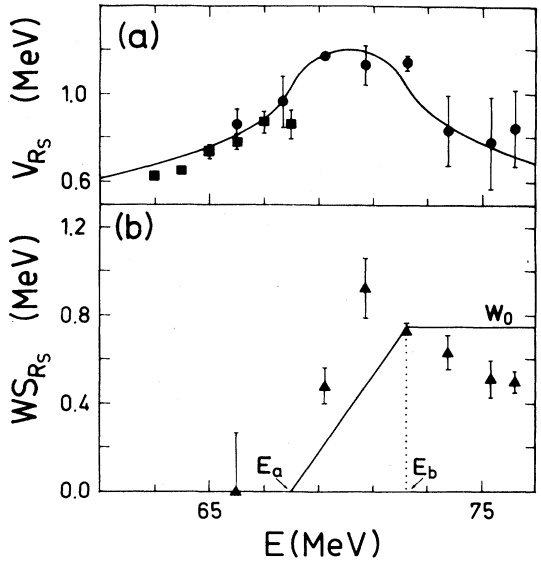

FIG. 7. Energy-dependent optical-model potential CP3 at the strong absorption radius ($R_s = 11.8$ fm). The lines are explained in the text. (a) Real part. (b) Imaginary part.

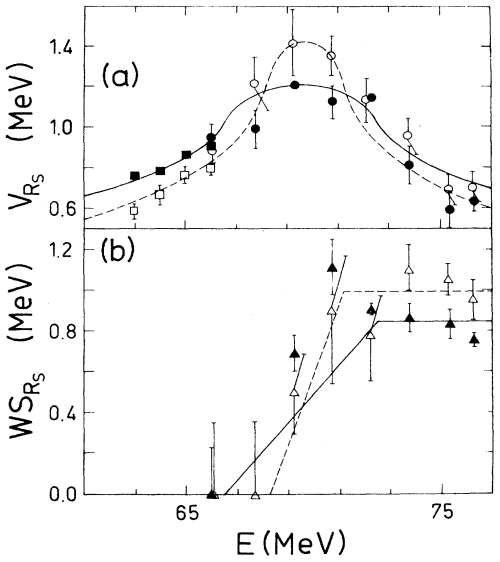

FIG. 8. Energy-dependent potentials for the optical model CP2 (solid symbols) and for coupled channels (open symbols) at the strong absorption radius ($R_s = 11.8$ fm). The lines are explained in the text. (a) Real part. (b) Imaginary part.

value of the real and imaginary parts of the optical potential, CP3, at the strong absorption radius. The error bars were determined by the change of the total χ^2 in one unit. However, since there is a correlation between the real and imaginary part of the potential for each energy they should only be taken as indicative. The solid line for $V_{R_s}(E)$ is obtained from the schematic dispersion relations, with E_a, E_b, and W_0 taken from Fig. 7(b) and normalized to the experimental value at 69.2 MeV. The squares in Fig. 7(a) correspond to the values of the real potential needed to adjust the fusion data when $WS = 0$. Table I shows the χ^2/point values obtained using for the real and imaginary parts of the optical potential the values corresponding to the solid lines of Figs. 7(a) and 7(b), respectively.

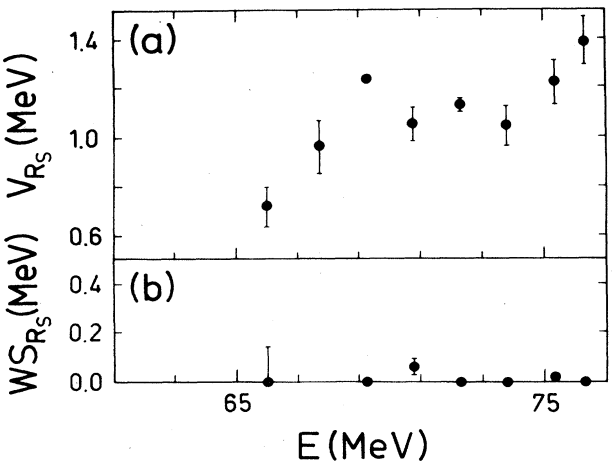

FIG. 9. Energy-dependent optical-model potential CP1 at the strong absorption radius ($R_s = 11.8$ fm).

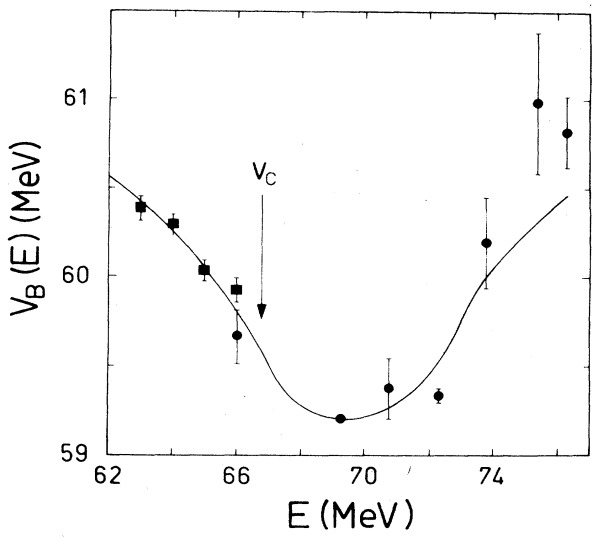

FIG. 10. Energy-dependent fusion barrier corresponding to the CP2 potential. The Coulomb barrier V_c is indicated.

A similar adjustment starting from RP2, and giving the potential CP2, is displayed in Figs. 8(a) and 8(b); the same overall behavior is observed and better values of χ^2/point are obtained (see Table I).

On the other hand, if the same procedure is started from RP1, giving the potential CP1, negligible values of *WS* are found. The real potential, however, does display an energy dependence, as shown in Fig. 9, which makes the discrepancy with the fusion data even worse.

In order to judge the agreement with the dispersion relations one should note that the bell-shaped energy-dependence characteristic of the real part of the potential is largely independent of the values of the imaginary part. In fact when *WS* is set equal to zero and the depths of the potentials RP2 and RP3 are allowed to change with energy, the values obtained for $V_{R_s}(E)$ are equal within error bars to the ones displayed in Fig. 7(a) and 8(a) (except for the points at 70.7 and 72.3 MeV which are lower by about 17%). Of course, the fits obtained forcing *WS* to be equal to zero are of worse quality (i.e., χ^2/point = 5.9 and 1.53 for the angular distributions at 72.3 and 69.2 MeV, respectively).

The effect of the energy dependence on fusion might be seen from a different standpoint by looking at the energy dependence of the one-dimensional fusion barrier parameters r_B, V_B, and $\hbar\omega$ obtained from the potential CP2. Each of these parameters changed by about 2% in the range of energies considered. The effect of these changes on fusion was estimated using Wong's model: fusion cross sections were found to depend only very mildly on r_B and $\hbar\omega$ whereas the dependence on V_B was significant. The variation of V_B with energy is shown in Fig. 10. Similar results are obtained for CP3.

IV. DWBA ANALYSIS

To describe the inelastic cross sections, separate DWBA calculations for the 2^+ and 3^- states in ^{144}Sm

TABLE II. Quality of the fits (χ^2/point) to inelastic scattering data from different potentials.

	χ^2/point			
	Angular distributions		Excitation functions	
Potential	69.2 MeV	72.3 MeV	137.1°	154.3°
RP0	14.1	7.5	2.6	3.9
RP1	8.5	35.5	8.2	2.2
RP2	7.1	16.5	1.3	0.4
RP3	7.2	18.0	2.2	0.2
CP2	2.1	0.9	1.0	0.4
CP3	3.3	1.6	1.4	0.3

were added incoherently. Runs were performed with the potentials of Table I.

The Coulomb deformation parameters of the 2^+ and 3^- states in ^{144}Sm were extracted from Ref. 19: $\beta_{c2}=0.088$ and $\beta_{c3}=0.121$. The nuclear deformation parameters were evaluated using the rolling model:

$$\beta_c R_c = \beta_n R_n$$

where $R_c = 1.2(A_p^{1/3} + A_t^{1/3})$, and $R_n = r_0(A_p^{1/3} + A_t^{1/3})$.

The results are shown in Figs. 3 and 5 and Table II. Even though the potential RP1 gives a good adjustment of the elastic data it performs poorly for the inelastic transitions. Again the best results are obtained with the energy-dependent potential CP2.

V. COUPLED-CHANNELS ANALYSIS

As mentioned in Sec. I, the ^{16}O+^{144}Sm system has been selected to minimize the influence of static and dynamic deformations. However, the consistent description of the data required the consideration of coupling to peripheral channels. These couplings were taken into account phenomenologically with energy-dependent imaginary and real potentials, tied together by dispersion relations. In principle, if all the important couplings were included explicitly, there would not be such a strong energy dependence. Since these calculations are very difficult to perform a truncated channel space must be used, and the need of using energy-dependent potentials would subsist. In this framework it is interesting to assess, how much the explicit consideration of some inelastic channels in a coupled-channels calculation affects the analysis presented in the previous sections.

Coupled-channels calculations were performed with the computer code PTOLEMY,[20] starting with the potential CP2 and the deformation parameters used in Sec. IV. The ground state was coupled to the lower-lying 2^+ and 3^- states in ^{144}Sm within the vibrational model. Test cases including the 4^+ state in ^{144}Sm and the 3^- state in ^{16}O were also run. This showed that the quality of the fits (χ^2/point) changed only by about 10% (20%) for the elastic (inelastic) angular distributions. Since the inclusion of these states was time consuming they were not considered in the final calculations.

The potential parameters V and WS were adjusted at each energy to obtain the best fit to both, the elastic and inelastic data. The imaginary potential WS in the excited states was taken equal to WS in the ground state at an energy shifted by the average excitation energy. Following the results for the uncoupled case (solid line of Fig. 8(b), the value of WS in the excited states, for energies below 72.5 MeV, was taken to be 65% of the value corresponding to the ground state, while for energies above 72.5 MeV both were equal. The geometry of the potentials was kept unchanged. The result of this search is displayed in Fig. 8, where the open symbols have the same meaning as in Sec. III B. The quality of the fits to elastic and inelastic angular distributions is somewhat worse than that obtained with CP2. In fact, the χ^2/point values for the elastic (inelastic) angular distributions at 66, 69.2, and 72.3 MeV are 0.46, 2.0 (1.2), and 1.3 (2.0), respectively.

The real potential V displays, at energies below the barrier, the well-known enhancing of the fusion cross sections due to coupling to inelastic states (a lower potential is enough in the coupling scheme to obtain the same cross section).

The imaginary potential WS is expected to decrease due to the explicit consideration of the inelastic channels. This occurs below 72.3 MeV but not above. Although this is not expected the determination of WS is uncertain since small changes on the adopted value of V would produce large variations on WS.

Even though the changes of V and WS with respect to the potential CP2 are small (about 20% for V and 35% for WS), their overall energy dependence seem to be more pronounced in both cases, in variance with expectations. Again the values of V and WS are in general agreement with the dispersion relations as is shown by the dashed lines of Fig. 8.

VI. SUMMARY AND CONCLUSIONS

Elastic and inelastic scattering in the ^{16}O+^{144}Sm system have been measured around the Coulomb barrier. These data plus existing fusion and elastic data have been analyzed within the framework of the optical model. It has been shown that with energy-independent optical potentials it was not possible to simultaneously describe fusion, elastic, and inelastic scattering data. Indeed, the potential that best adjusts the fusion data (RP0) fails to reproduce the elastic data, whereas the one which best adjusts the elastic data (RP1) fails to reproduce the fusion data.

On the other hand, energy-dependent potentials, consistent with the dispersion relations, give very good account of elastic, inelastic, and fusion data. The real part of these energy-dependent potentials is well determined,

but the imaginary surface potential is less certain. Further work is in progress to reduce this uncertainty by requiring in addition that the surface imaginary potential give account of the peripheral processes. The explicit consideration of couplings to the 2^+ and 3^- states in ^{144}Sm, produces small changes in the potentials which are again consistent with the dispersion relations.

In the framework of the optical model, the surface imaginary potential simulates the effect of transfer and inelastic channels. The closure of these channels at energies below the barrier produces, according with the dispersion relations, an energy dependence of the real potential as discussed in Sec. III B. In turn, this energy dependence causes the potential barrier to change near the Coulomb barrier region, allowing a coherent description of scattering and fusion data.

This work has been supported in part by the Consejo Nacional de Investigaciones Científicas y Técnicas, Argentina.

[1] *Fusion Reactions Below the Coulomb Barrier,* Vol. 219 of *Lecture Notes in Physics,* edited by S. G. Steadman (Springer-Verlag, Heidelberg, 1985).

[2] W. Reisdorf, in *Proceedings of the International Nuclear Physics Conference, Harrogate, 1986,* edited by J. L. Durell *et al.* (Institute of Physics, Bristol, 1987), Vol. 2, p. 205.

[3] M. J. Rhoades-Brown and P. Braun-Munzinger, Phys. Lett. **136B**, 19 (1984).

[4] C. H. Dasso, S.Landowne, and A. Winther, Nucl. Phys. **A405**, 381 (1983).

[5] S. C. Pieper, M. J. Rhoades-Brown, and S. Landowne, Phys. Lett. **162B**, 43 (1985).

[6] R. G. Stokstad and E. E. Gross, Phys. Rev. C **23**, 281 (1981).

[7] D. E. DiGregorio, J. O. Fernandez Niello, A. J. Pacheco, D. Abriola, S. Gil, A. O. Macchiavelli, J. E. Testoni, P. R. Pascholati, V. R. Vanin, R. Liguori Neto, N. Carlin Filho, M. M. Coimbra, P. R. Silveira Gomes, and R. G. Stokstad, Phys. Lett. B **176**, 322 (1986).

[8] W. Reisdorf, F. P. Hessberger, K. D. Hildenbrand, S. Hofmann, G. Münzenberg, K. H. Schmidt, J. H. R. Schneider, W. F. N. Schneider, K. Sümmerer, G. Wirth, J. V. Kratz, and K. Schlitt, Phys. Rev. Lett. **49**, 1811 (1982).

[9] M. J. Rhoades-Brown and M. Prakash, Phys. Rev. Lett. **53**, 333 (1984).

[10] J. S. Lilley, B. R. Fulton, M. A. Nagarajan, I. J. Thompson, and D. W. Barnes, Phys. Lett. **151B**, 181 (1985).

[11] B. R. Fulton, D. W. Barnes, J. S. Lilley, M. A. Nagarajan, and I. J. Thompson, Phys. Lett. **162B**, 55 (1985).

[12] C. Mahaux, H. Ngô and G. R. Satchler, Nucl. Phys. **A449**, 354 (1986).

[13] A. J. Pacheco, A. O. Macchiavelli, D. Abriola, D. E. DiGregorio, A. Etchegoyen, M. C. Etchegoyen, J. O. Fernandez Niello, A. M. J. Ferrero, S. Gil, J. A. Kittl, and J. E. Testoni, Z. Phys. (in press).

[14] P. Talon, N. Alamanos, M. Lameki-Rachti, C. Levi, and L. Papineau, Nucl. Phys. **A359**, 493 (1981).

[15] C. Y. Wong, Phys. Rev. Lett. **31**, 766 (1973).

[16] O. Akyüz and A. Winther, in Proceedings of the International School of Physics "Enrico Fermi," Course LXXVII, Varenna, 1979, edited by R. A. Broglia and R. A. Ricci (North-Holland, Amsterdam, 1981), p. 492.

[17] In this case, the strong absorption radius is equal within errors to the average distance at which the optical-model fits are sensitive (Ref. 11). The sensitive-distance change from 11.6 to 12.1 fm for $E = 66$ to 76.3 MeV, respectively.

[18] J. A. Kittl, J. E. Testoni, A. O. Macchiavelli, A. J. Pacheco, D. Abriola, D. E. DiGregorio, A. Etchegoyen, M. C. Etchegoyen, J. O. Fernandez Niello, A. M. J. Ferrero, and S. Gil, Nucl. Phys. **A471**, 587 (1987).

[19] G. Pálla, H. V. Geramb, and C. Pegel, Nucl. Phys. **A403**, 134 (1983).

[20] M. J. Rhoades-Brown, M. H. Macfarlane, and S. C. Pieper, Phys. Rev. C **21**, 2417 (1980).